The Company of Biologists

TOOLS AND TECHNIQUES

A quantitative FastFUCCI assay defines cell cycle dynamics at a single-cell level

Siang-Boon Koh[1,*], Patrice Mascalchi[1,2], Esther Rodriguez[1], Yao Lin[1,3], Duncan I. Jodrell[1], Frances M. Richards[1,*] and Scott K. Lyons[1,4]

ABSTRACT

The fluorescence ubiquitination-based cell cycle indicator (FUCCI) is a powerful tool for use in live cells but current FUCCI-based assays have limited throughput in terms of image processing and quantification. Here, we developed a lentiviral system that rapidly introduced FUCCI transgenes into cells by using an all-in-one expression cassette, FastFUCCI. The approach alleviated the need for sequential transduction and characterisation, improving labelling efficiency. We coupled the system to an automated imaging workflow capable of handling large datasets. The integrated assay enabled analyses of single-cell readouts at high spatiotemporal resolution. With the assay, we captured in detail the cell cycle alterations induced by antimitotic agents. We found that treated cells accumulated at G2 or M phase but eventually advanced through mitosis into the next interphase, where the majority of cell death occurred, irrespective of the preceding mitotic phenotype. Some cells appeared viable after mitotic slippage, and a fraction of them subsequently re-entered S phase. Accordingly, we found evidence that targeting the DNA replication origin activity sensitised cells to paclitaxel. In summary, we demonstrate the utility of the FastFUCCI assay for quantifying spatiotemporal dynamics and identify its potential in preclinical drug development.

KEY WORDS: Automated microscopy, DNA replication origin, Drug synergy, FUCCI, Live-cell imaging, Taxane

INTRODUCTION

The fluorescence ubiquitination-based cell cycle indicator (FUCCI) system represents a quantum leap for real-time examination of cell cycle progression (Sakaue-Sawano et al., 2008). This technology relies on the choreography of two players of the DNA replication control apparatus, the licensing factor CDT1 and its inhibitor geminin (Zielke and Edgar, 2015). In eukaryotic cells, CDT1 level peaks during G1 and plummets upon S entry. Conversely, the geminin level is high during S and G2 but is low during late mitosis and G1. The alternating expression of these two proteins arises from the sequential activation of the E3 ubiquitin ligases SCF[Skp2] (a Skp1–cullin-1–F-box complex that contains Skp2 as the F-box

protein), and the anaphase-promoting complex/cyclosome (APC/C), which target the degradation of CDT1 and geminin, respectively. By fusing fluorescent proteins to degrons derived from CDT1 and geminin, the FUCCI system thus enables continuous visualisation of live cells in either G1 or the S- and/or G2-to-M phases (hereafter denoted as S/G2-M).

To date, various FUCCI-based laboratory models have been employed together with live-cell imaging to elucidate the effects of therapeutic modulation (Sakaue-Sawano et al., 2011; Yano et al., 2013; Dan et al., 2012; Koh et al., 2015). However, despite the detailed molecular insights one can gain from such imaging, the approach remains uncommon owing to its technical complexity. In particular, advances in automated imaging hardware have not been matched by the ease and accessibility of multiparametric image-based processing workflows. As a result, many live-cell assays are not designed with good throughput capability and often depend on manual handling of a limited number of datasets (Chirieleison et al., 2011; Boutros et al., 2015; Singh et al., 2014).

Here, we developed a rapid selectable lentiviral-based system called FastFUCCI that allowed simultaneous introduction of both FUCCI transgenes, that is the CDT1- and geminin-tagged reporters, into cells. The method alleviated the conventional requirement for sequential cell line transduction and characterisation, thereby improving labelling efficiency. We coupled the FastFUCCI system to a cascade of image acquisition, processing and analysis streamlined for the single-cell level. This was achieved by developing a versatile live-cell assay implemented in a modular design, where each handling step was independently scalable and automated by open-source scripts. A key feature of this assay was its ability to perform batch management of high-volume data; the quantitative output of these data was image-based and therefore amenable to downstream validation.

To demonstrate the utility of the FastFUCCI imaging assay, we applied it to define the cellular and molecular events in cancer cells following treatment with antimitotic agents. Antimitotic agents such as taxanes are frequently used for cancer treatment. These agents disrupt mitotic progression, resulting in structural aberrations that in turn elicit mitotic arrest. Although the mechanism of these events is well described, comparatively little is known about how cells respond to such insults spatiotemporally (Gascoigne and Taylor, 2009; Rieder and Maiato, 2004). To this end, we first monitored the cell cycle dynamics at the single-cell level in response to treatment with varying concentrations of paclitaxel and nocodazole. We then correlated the cell cycle distributions with the temporal dimension, as quantified by single-cell tracking of the different cell cycle phases. Using the FastFUCCI assay revealed actionable spatiotemporal effects induced by antimitotic agents, leading to evidence that co-targeting mitosis and the DNA replication origin activity was a potential therapeutic strategy.

[1]Cancer Research UK Cambridge Institute, University of Cambridge, Li Ka Shing Centre, Robinson Way, Cambridge CB2 0RE, UK. [2]Bordeaux Imaging Center, UMS 3420 CNRS-Université de Bordeaux-US4 INSERM, Pôle d'imagerie photonique, Bordeaux F-33000, France. [3]College of Life Sciences, Fujian Normal University, Fujian 350117, P. R. China. [4]Cold Spring Harbor Laboratory, 1 Bungtown Road, New York 11724, US.

*Author for correspondence (siangboon.koh@cantab.net; fran.richards@cruk.cam.ac.uk)

S.-B.K., 0000-0002-5494-3800

RESULTS

Stable generation of the FastFUCCI reporter system

Traditional generation of a FUCCI-expressing cell line entails sequential expression of the two FUCCI reporters, CDT1 and geminin. To simplify this procedure, we directed the simultaneous expression of both reporters in equimolar amounts by cloning both transgenes [monomeric Kusabira Orange 2 (mKO2)–hCDT1(30–120) and monomeric Azami Green (mAG)–hGEM(1–110), where m denotes mouse and h denotes human], separated by a T2A sequence, downstream of a single EF1α promoter. This expression cassette was subsequently cloned into the lentiviral backbone pBOB to permit fast generation of a cell population that stably expressed both FUCCI reporters (Fig. 1A; Fig. S1, Table S1).

We introduced the expression of both FUCCI reporters in human pancreatic cancer MIA PaCa-2 cells through lentiviral transduction. In stably transduced cells, fluorescence was observed in the nuclei, and both red (mKO2) and green (mAG) signals alternated predictably according to the phases of the cell cycle (Fig. 1B). Flow cytometric analysis shows comparable cell cycle distributions in both parental and FastFUCCI-expressing cells (Fig. 1C). The red-, yellow- and green-emitting populations in the latter corresponded to cells in G1, the G1/S transition and S/G2-M, respectively.

### Automated extraction of FastFUCCI time-lapse data

The increasing use of multiparametric microscopy assays has demanded workflows that can manage practical issues related to processing and analysis of large datasets (Singh et al., 2014). To acquire and analyse time-lapse data in an unbiased and automated fashion, we proceeded to develop the FastFUCCI imaging assay (Fig. 2A; Fig. S2A,B). We streamlined the assay with automation at each principal step to afford user-independent handling of a high number of images. The output was time-lapse data with consistent image resolution and contrast, allowing downstream analyses to be performed in batch mode by commercial and open-source image analysis platforms, as tested with the Columbus™ Image Data Storage and Analysis and Fiji, respectively, in this work (Fig. 2A).

To demonstrate these functional features, we performed a 12-h study on the FastFUCCI-expressing MIA PaCa-2 cells treated with the previously characterised CDK1-selective inhibitor RO3306, which was expected to arrest cells at the G2/M boundary (Vassilev et al., 2006). CDK1 inhibition induced a dose-dependent increase in the green population and a corresponding decrease in the red population (Fig. 2B). Consistent with previous studies, this effect on single-cell spatiotemporal dynamics was rapid, as the apparent difference was noticeable as early as 1 h following treatment, reflecting an accumulation of S/G2-M cells (Vassilev et al., 2006; Marcus et al., 2015). Automated single-cell duration measurement showed that the increase in the S/G2-M population was correlated with the residence time in the green phase (representing this population), the latter also exhibiting a dose-dependent trend (Fig. 2C).

Real-time monitoring of cell cycle modulation by antimitotic agents

We exploited the assay to define the single-cell spatiotemporal dynamics induced by paclitaxel at high definition. Based on the IC_{50} of paclitaxel (4.7 ± 0.3 nM; mean±s.e.m.) (Fig. 3A), we subjected FastFUCCI-expressing MIA PaCa-2 cells to a low (3 nM) and a high (30 nM) concentration of paclitaxel. Cell cycle progression was monitored, with total number of cells being taken as a parameter for proliferation (Fig. 3B–E). We found that, in the vehicle control, the fractions of red and green cells each displayed a reciprocally oscillating profile as total cell count increased over time, in line with the predicted behaviour of cycling single cells (Fig. 3B,C). In 3 nM paclitaxel, the alternating oscillation remained evident, with minimal changes in the cell cycle distributions consistent with the minimal inhibition of proliferation (Fig. 3B,D). In contrast, in
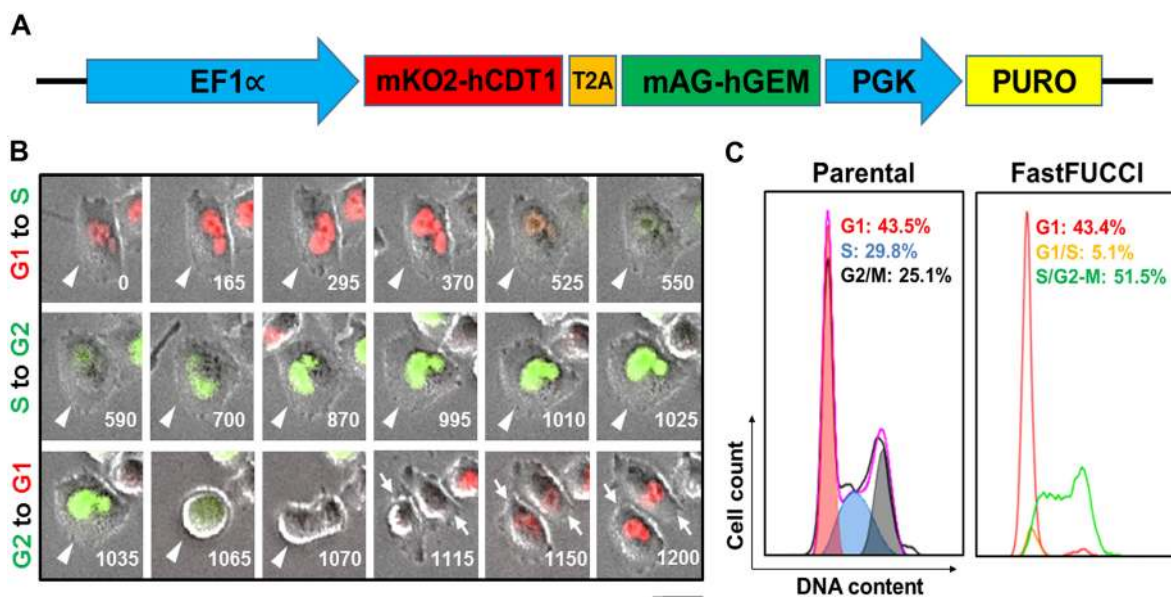
Fig. 1. Generation of the FastFUCCI model. (A) Design of the pBOB-EF1-FastFUCCI-Puro construct. See Fig. S1 for full map of the construct, and Table S1 for all single and two-cutter 6+ nucleotide restriction enzymes with respective positions and actual nucleotide numbers. (B) Cell-cycle-dependent changes in fluorescence in a FastFUCCI-expressing MIA PaCa-2 cell. The arrowhead denotes the mother cell that was tracked; arrows denote daughter cells arising from the tracked mother cell. The number denotes time in minutes. Scale bar: 25 µm. (C) Cell cycle profile of parental and FastFUCCI-expressing MIA PaCa-2 cells harvested in exponential growth, measured by flow cytometry. The Dean-Jett-Fox model was used to quantify G1, S and G2 and M (G2/M) fractions of the parental line, based on DNA content as measured by DAPI. The FUCCI indicators were used to quantify the G1, G1/S transition and S/G2-M fractions of the FastFUCCI line.
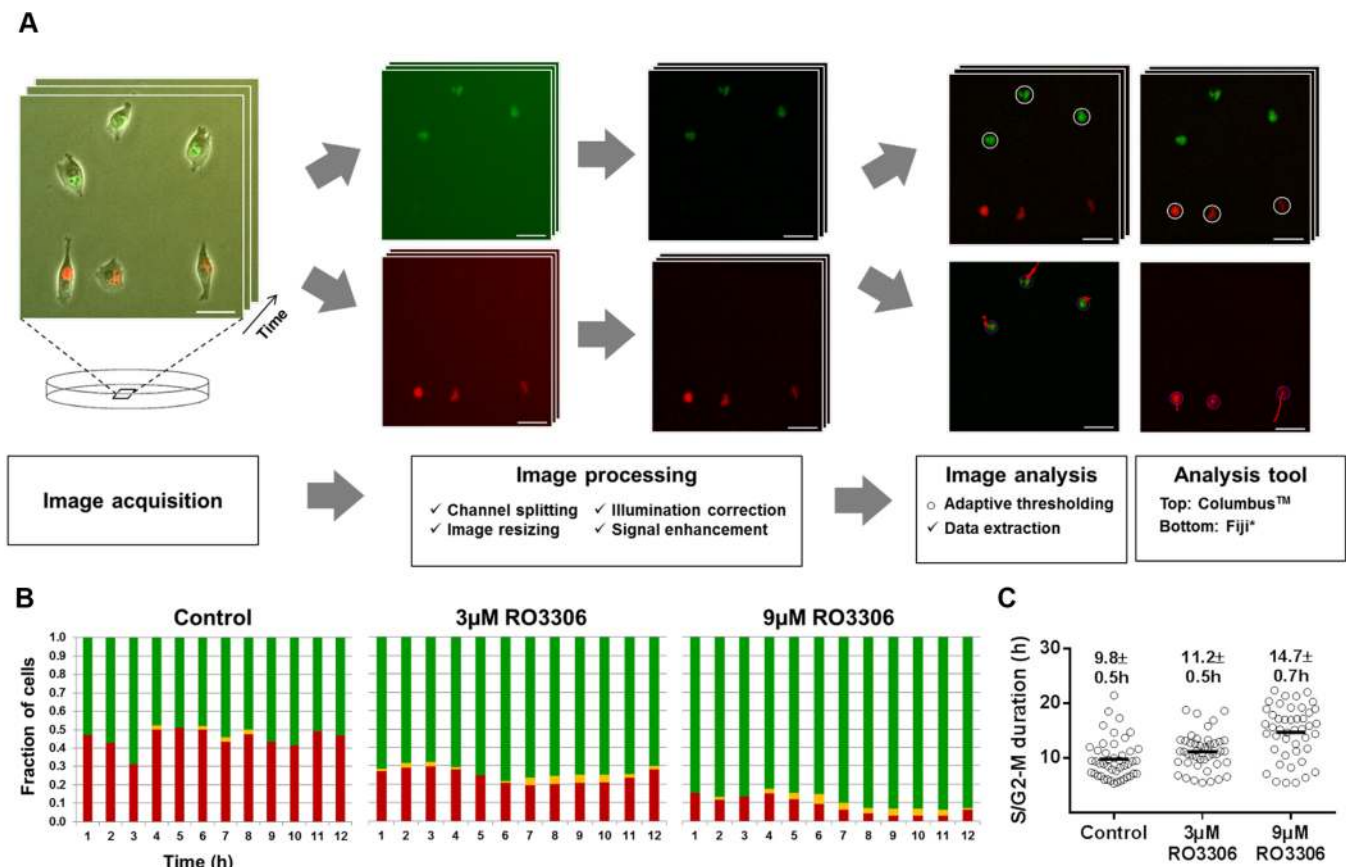
Fig. 2. Automated image processing and analysis. (A) Schematic for the FastFUCCI imaging assay with examples of still images obtained from the automated platform. Scale bar: 40 µm. See Materials and Methods for full details. Briefly, image processing involved colour-channel separation, data resizing, illumination adjustment and improvement of the signal-to-noise ratio. Image analysis involved threshold setting and data extraction, such as object scoring and event quantification. Ticks denote that the step was automated; open circle denotes that the step required user input. *Other compatible open-source packages include CellCognition, CellProfiler and CellProfiler Analyst, and EBImage. (B) Image-based cell cycle profiling. FastFUCCI-expressing MIA PaCa-2 cells were treated as indicated and were imaged for 12 h. Fractions of red, green and yellow cells were quantified using the Columbus™ software. Data shown were from three fields of view per time point, with a mean total of 313 cells per condition scored. (C) The S/G2-M duration of FastFUCCI-expressing MIA PaCa-2 cells treated as indicated, analysed using the Fiji software. Duration is reported as mean±s.e.m., n=45 cells per condition, collected from imaging for 24 h after drug addition.

30 nM paclitaxel, there was an initial accumulation of the green fraction up to 6 h (Fig. 3E). From 6 to 24 h, the green fraction decreased with a concomitant rise in the red fraction, implying that the initial mitotic arrest was followed by either mitotic death or mitotic slippage (the process by which cells proceed through mitosis to interphase without chromosome segregation). Given that cell proliferation did not appear to decline until after 24 h, this suggests that there was mitotic slippage, rather than extensive death in mitosis (Fig. 3B). Similar observations were made in paclitaxel-treated FastFUCCI-expressing Panc-1 cells, where accumulation of green cells was followed by accumulation of red cells (Fig. S3A–C).

To correlate the spatiotemporal dynamics with cell cycle residence time, we quantified the cell cycle durations of individual FastFUCCI-expressing MIA PaCa-2 cells under the same conditions (Fig. 3F,G). In control, the average S/G2-M duration was 8.9±0.2 h (mean± s.e.m.), comparable with previous results (Koh et al., 2015). Cells treated with 3 nM paclitaxel experienced similar S/G2-M duration (9.7±0.3 h), whereas those treated with 30 nM paclitaxel had almost double the duration (16.1±0.6 h) compared to control. The dose-dependent delay in S/G2-M was correlated with G1 prolongation (Fig. 3G). All these effects on cell cycle dynamics were similarly observed with nocodazole, another mitotic inhibitor, indicating that the findings were not specific to taxanes (Fig. S3D–H).

Spatiotemporal analysis of taxane-induced cell death

The temporal dichotomy of the red and green fractions induced by the antimitotic agents prompted us to use the FastFUCCI system to determine the basis of their cytotoxicity (Fig. 3E; Fig. S3C,F). First, we performed manual cell fate analysis of 30 nM paclitaxel-treated FastFUCCI-expressing MIA PaCa-2 cells (Fig. 4A). Of the 190 randomly selected cells tracked for 72 h, all of them attempted mitosis, with 2% eliminated during mitosis. In the remaining 98%, three distinct mitotic phenotypes were identified: abortive mitosis (no daughter, 57%), bipolar mitosis (two daughters, 32%), multipolar division (three or more daughters, 9%).

Next, we determined the ensuing fate of cells that had progressed through mitosis into the second cell cycle (Fig. 4B). Independent of the nature of the preceding mitotic phenotype, the majority of these cells (73–75%) died in the red phase (i.e. G1). An important observation was that some of these cells arrived at the red phase without overt reflattening before death and appeared morphologically similar to those that underwent mitotic death in green phase (Fig. 4C). The remaining fraction either died in the next green phase (10–15%) or appeared to remain alive (12–16%) (Fig. 4B).

To substantiate these live-cell FastFUCCI analyses, we performed quantitative immunofluorescence of MIA PaCa-2 cells
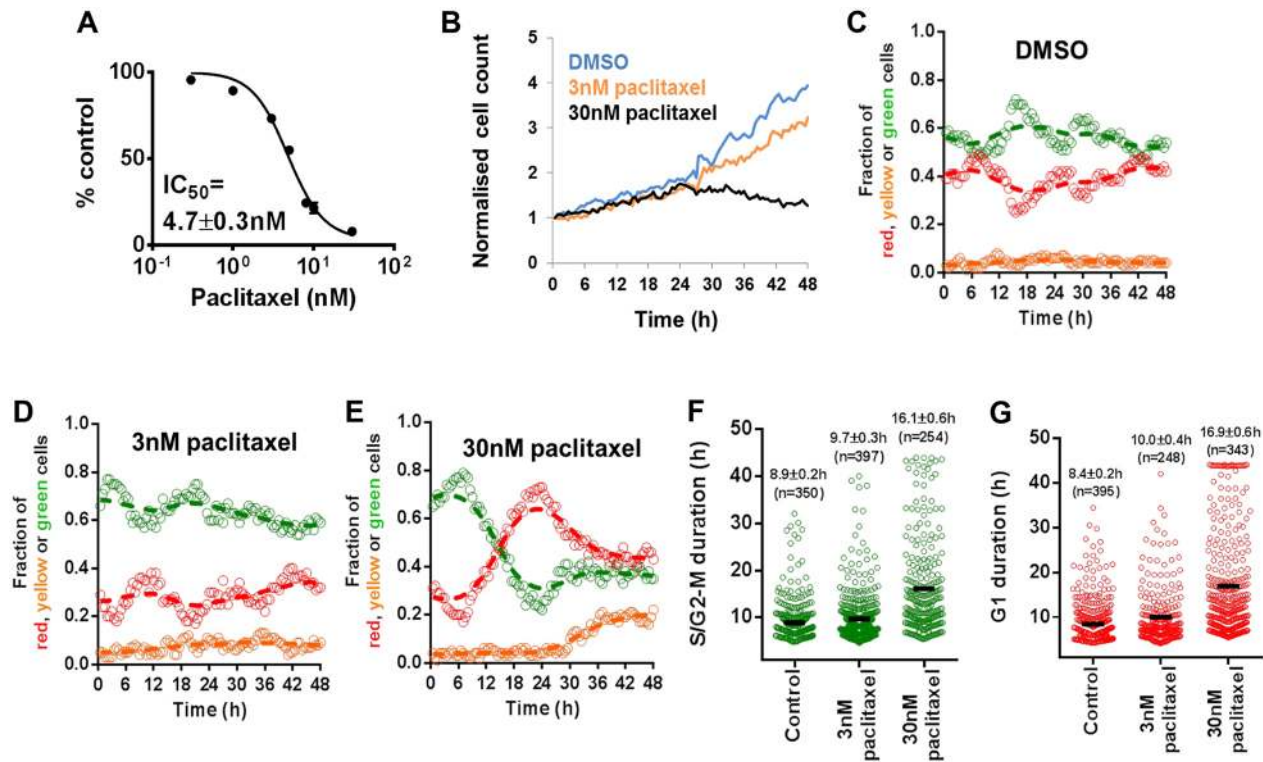
Fig. 3. Real-time quantification of cell cycle modulation in paclitaxel-treated cells. (A) Dose–response curve for paclitaxel in parental MIA PaCa-2 cells treated for 72 h as measured by a sulforhodamine B assay. Cell growth at the time of treatment (time zero) was subtracted from all samples and growth inhibition was calculated by expressing it as a ratio of the mean of DMSO control. IC_{50} is reported as the mean±s.e.m., $n=4$. (B) Real-time monitoring of single-cell count. FastFUCCI-expressing MIA PaCa-2 cells were treated as indicated and cell number was quantified every 30 min. Data shown were from three fields of view per time-point, and each value was normalised to the initial cell count. (C–E) Fractions of red, green and yellow cells in samples treated as in B. Data shown were from three fields of view per time-point, with a mean total of 17,816 cells per condition scored. (F) S/G2-M and (G) G1 duration of individual FastFUCCI-expressing MIA PaCa-2 cells treated as indicated. Duration is reported as mean±s.e.m., n=number of cells, collected from imaging for 72 h after drug addition.

to enumerate the proportion of cells that were dead or dying in mitosis. We employed cleaved caspase 3 (c-caspase 3) and cyclin B1 as markers of apoptosis and mitosis, respectively (Fig. 5A). Irrespective of treatment duration (0–48 h), we found that less than 30% of c-caspase-3-positive cells were positive for cyclin B1 (Fig. 5B). Validation using another apoptotic (γH2AX) and mitotic (pHH3) markers yielded the same conclusion – that mitosis was not the main phase in which cell death occurred (Fig. 5C,D; Fig. S4A). All these results were verified in Panc-1 cells (Fig. S4B–D).

### Interaction between taxanes and DNA replication origin inhibitors

Our findings suggest that post-mitotic entry into subsequent interphase is important for maximal paclitaxel cytotoxicity. To test this hypothesis, we performed a series of scheduled washout experiments on MIA PaCa-2 cells (Fig. 6A). We found that there was a duration-dependent decrease in proliferation index compared to time-matched controls (Fig. 6B). When the incubation time for 30 nM paclitaxel was limited up to 12 h (i.e. before the red fraction overtook the green fraction in Fig. 3E), the proliferation index remained above unity, indicating that cells had proliferated. A 24-h incubation largely prevented subsequent proliferation whereas a 48-h incubation had a killing effect, consistent with the total cell count dynamics in Fig. 3B.

Whereas drug incubation of at least 24 h appeared necessary for short-term growth suppression, from the fraction of cells that remained viable even following a 3-day treatment (Fig. 4B), 26% subsequently re-entered S phase (Fig. 6C). Based on the paradigm

that re-entry into active cell cycle could underlie chemoresistance, we investigated whether inhibiting the DNA replication origin firing following paclitaxel treatment could improve chemosensitisation. We performed long-term cell proliferation studies, where we pretreated MIA PaCa-2 cells with 30 nM paclitaxel for 24 h and released viable cells into roscovitine, a pan-CDK inhibitor commonly used to suppress origin activity. As expected, we found that 24-h paclitaxel pretreatment impaired but did not obliterate proliferation compared to DMSO control (Fig. 6D,E). Additional treatment with roscovitine further reduced the proliferative capacity compared to the Bliss-predicted additivity value, suggesting an apparent synergistic interaction. Replacement of roscovitine with PHA767491 to inhibit CDC7, another replication origin regulator, reproduced this potential synergistic relationship with paclitaxel pretreatment. Similar results were obtained in Panc-1 cells (Fig. 6D,E).

DISCUSSION

Devising methods to visualise single-cell states is an area of active development (Walling and Shepard, 2011). In particular, as interest in multiparametric imaging assays grows, the need for efficient workflows that encompass data acquisition, processing and analysis has become more evident (Chirieleison et al., 2011; Singh et al., 2014). Here, we developed a selectable lentiviral reagent that enables rapid expression of the two FUCCI reporter transgenes in cells. We applied this FastFUCCI system to a streamlined imaging workflow that performs automated image processing and analysis. Practically, the FastFUCCI imaging workflow is supported by
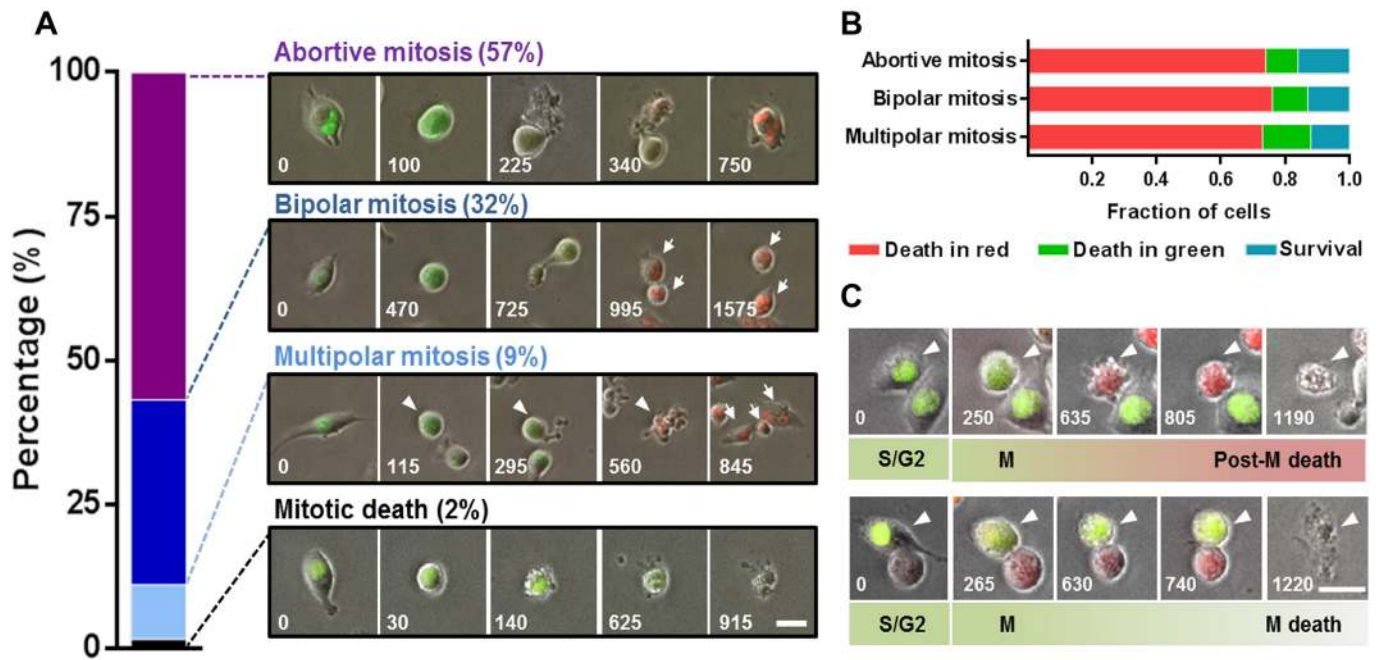
Fig. 4. Single-cell fate analysis following paclitaxel treatment. (A) Examples of FastFUCCI-expressing MIA PaCa-2 cell fate following treatment with 30 nM paclitaxel. The arrowhead denotes the mother cell that was tracked; arrows denote daughters cell arising from the tracked mother cell. The number denotes time in minutes. A total of 190 cells from two independent experiments were analysed. Scale bar: 25 µm. (B) Fraction of cells treated with 30 nM paclitaxel for 3 days that had died in the subsequent red or green phase, or had remained alive following abortive, bipolar or multipolar mitosis. A total of 285 cells from two independent experiments were analysed. (C) Examples of cell undergoing death in the red phase (top panel) and mitotic death (bottom panel). The arrowhead denotes cell that was tracked. The number denotes time in minute. Scale bar: 25 µm.

open-source scripts and is modular in its construction, with the output being digital images of accessible format (TIFF). Hence, it is amenable to current commercial and open-source image analysis programmes, as demonstrated here by its coupling with the Columbus™ and Fiji software, respectively. Analytically, the workflow enables quantification of large numbers of images,
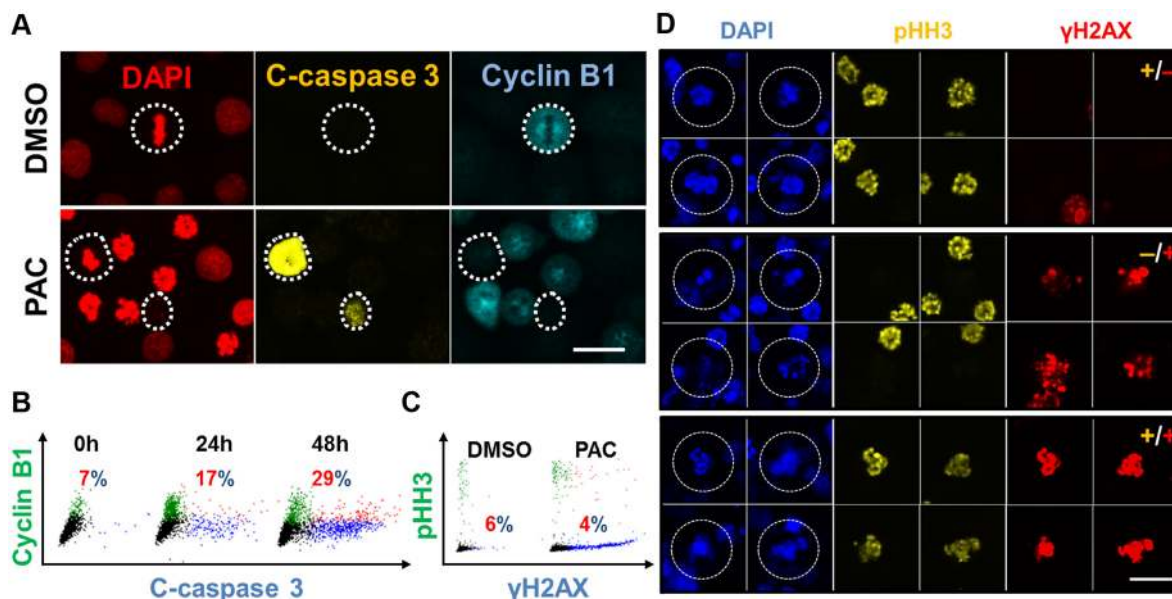
Fig. 5. Correlation of paclitaxel-induced cell death and mitosis. (A) Immunofluorescence of parental MIA PaCa-2 cells treated with vehicle (DMSO, top panel) or 30 nM paclitaxel (PAC, bottom panel) for 24 h. Dashed circles indicate cells that stain for either c-caspase-3 or cyclin B1. The cell in the middle of the bottom panel was apoptotic with a highly fragmented nucleus. Scale bar: 25 µm. (B) Quantification of parental MIA PaCa-2 cells treated with 30 nM paclitaxel over the course of 48 h. Each dot represents a single cell; black dots denote negative cells, blue dots denote c-caspase-3-positive cells, green dots denote cyclin-B1-positive cells, red dots denote c-caspase 3 and cyclin B1 double-positive cells. The number denotes the percentage of c-caspase-3-positive cells that were positive for cyclin B1. A total of >2000 single cells per time point were scored. (C) Quantification of parental MIA PaCa-2 cells treated with vehicle or 30 nM paclitaxel for 48 h. Each dot represents a single cell: black dots denote negative cells, blue dots denote γH2AX-positive cells, green dots denote phosphorylated histone H3 (pHH3)-positive cells, red dots denote γH2AX and pHH3 double-positive cells. The number denotes the percentage of γH2AX-positive cells that were positive for pHH3. A total of >2000 single cells per condition were scored. (D) Examples (circles) of paclitaxel-treated MIA PaCa-2 cells in C. Scale bar: 25 µm.
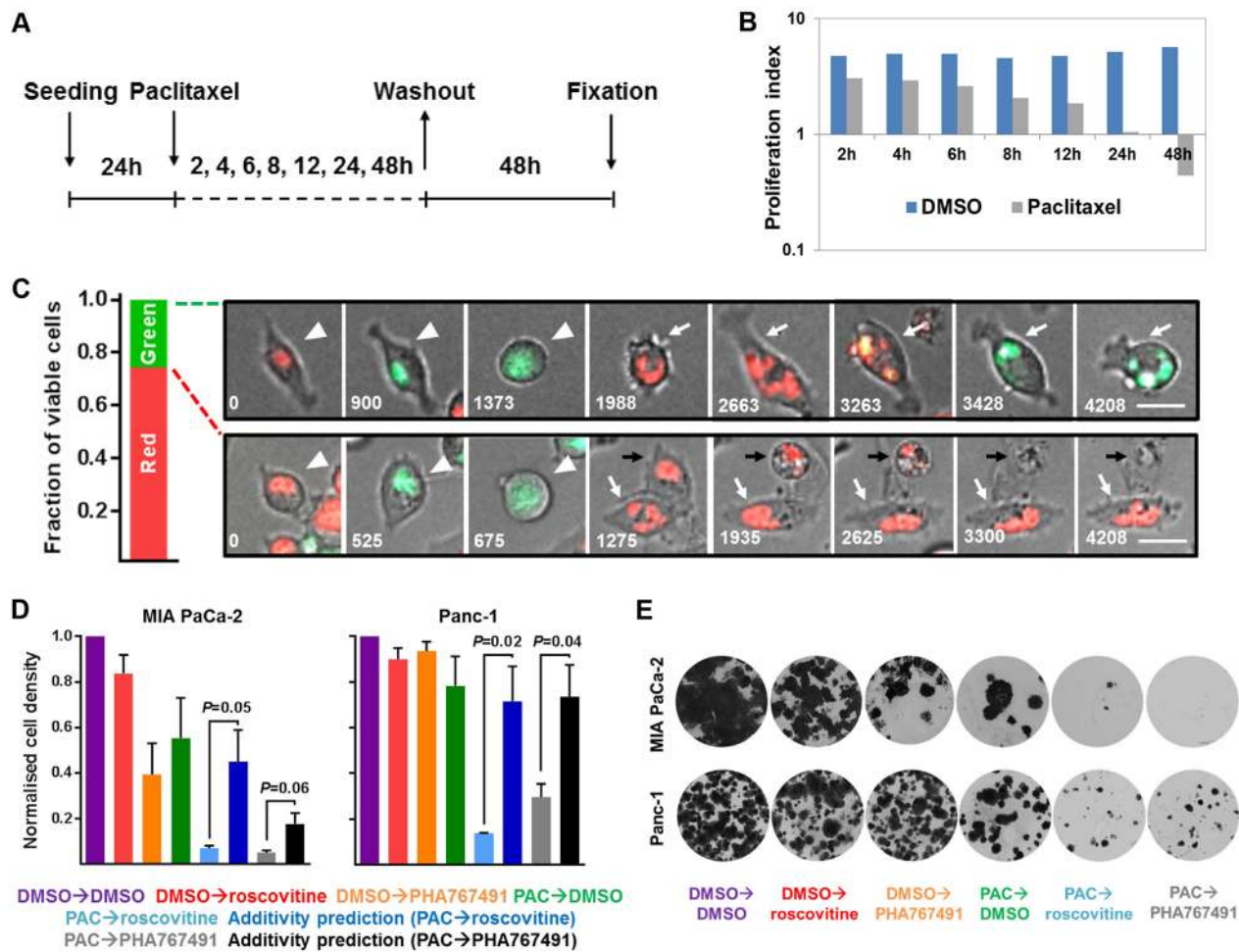
Fig. 6. Interaction between paclitaxel and DNA replication origin inhibitors. (A) Schematic for scheduled washout experiments. 30 nM paclitaxel was washed out after a specified duration, and parental MIA PaCa-2 cells were left to grow in fresh medium for 48 h. (B) Proliferation assays for the washout experiments illustrated in A. Sulforhodamine B staining was used to determine proliferation indices, which were calculated from the ratio of cell number after the 48-h fresh medium incubation to cell number at the time of treatment (time zero). (C) Quantification of the viable fraction of FastFUCCI-expressing MIA PaCa-2 cells in Fig. 4B. The top panel shows an example of a cell undergoing abortive mitosis (arrowhead) and subsequently entering the green phase (arrow). The bottom panel shows an example of a mother cell undergoing bipolar mitosis (arrowhead), with one daughter that eventually died (black arrow) and one daughter that appeared alive in the red phase (white arrow). The number denotes time in minute. Scale bar: 25 µm. (D,E) Long-term cell proliferation studies. Parental MIA PaCa-2 or Panc-1 cells were treated with 30 nM paclitaxel (PAC) for 24 h. Viable cells were then released into DMSO, 8 µM roscovitine or 2 µM PHA767491 and were left to grow for 2 weeks. Crystal Violet absorbance was normalised to that of vehicle control. Data are represented as mean±s.e.m., n=3. A two-tailed t-test was used to calculate the indicated P-value between the combination results and corresponding Bliss additivity prediction. See Materials and Methods for additivity prediction calculation.

objects or events, conferring the statistical power necessary to detect subtle, transient or rapid real-time dynamics (Hamilton, 2009). Extraction of multidimensional data at such a scale would be a resource for studies attempting to integrate the FUCCI technology with mathematical modelling (Saitou and Imamura, 2016). Equally, addition of other imaging features, such as shape recognition, to the workflow would further diversify its experimental applications.

To test the utility of the FastFUCCI imaging assay, we applied it to dissect the spatiotemporal effects induced by antimitotic agents. Earlier studies had attempted to establish a link between paclitaxel-induced cell death and mitotic exit, but it remained unclear if mitotic exit represented a major pro-death event (Bekier et al., 2009; Tao et al., 2005; Gascoigne and Taylor, 2008; Shi et al., 2008; Huang et al., 2009; Orth et al., 2008). Although the ambiguity might have stemmed from interline variation, the understanding so far has been drawn from cell-population-based experiments, phase-contrast

images or low-content microscopy, precluding the precise discrimination between cells that die in mitosis and cells that die following a mitotic attempt. More recently, several qualitative studies using FUCCI-expressing cells have reported the emergence of CDT1 expression following prolonged mitosis (Honda-Uezono et al., 2012; Kaida et al., 2011; Marcus et al., 2015). Through in-depth single-cell analyses, we found this phenomenon to be far more common than previously implied. Importantly, we forged a quantitative association between post-mitotic entry and cell death, the latter being independent of the mitotic phenotype. Our results are supported by previous studies that investigated the role of post-mitotic entry in finalising apoptosis (Tao et al., 2005; Orth et al., 2012). Further mechanistic studies are warranted to elucidate how mitotic arrest and subsequent interphase entry differentially engage the resolution of death.

Three therapeutic considerations arise from this work. First, conventional regimens are often based on the principle of maximum

tolerable doses (Marshall, 2012). We have shown that, even at a cytotoxic concentration that elicits growth inhibition, cancer cells do regain some extent of proliferative capacity when drug residence falls below a critical threshold, that is when cells have not yet progressed beyond mitosis and become committed to apoptosis. This suggests that paclitaxel sensitivity depends not only on the strength of the mitotic checkpoint but also on the extent of checkpoint adaptation (Weaver and Cleveland, 2005). An understanding of how these mechanisms enact *in vivo* in relation to drug pharmacokinetics would inform future development of the recently proposed adaptive strategy for paclitaxel (Enriquez-Navas et al., 2016).

Second, our *in vitro* data using pancreatic cancer cell lines recapitulate the phenomenon seen in a fibrosarcoma xenograft model, whereby cancer cells accumulate in G1 following paclitaxel-induced mitotic arrest (Chittajallu et al., 2015). Our high-definition spatiotemporal analyses indicate that a large fraction of these cells are the direct consequence of treatment, having progressed through aberrant mitosis into G1 (Vakifahmetoglu et al., 2008; Shi et al., 2008). Some of these cells appear viable, and most of them stay in G1, presumably in an arrested or senescent mode. However, a few of the survivors subsequently re-enter S phase. It is conceivable that acquired resistance might arise from these cells that have been therapeutically challenged but do not succumb (Ogden et al., 2015).

Third, a second agent that targets the surviving post-mitotic population might confer further chemosensitisation. We demonstrated this possibility with the synergistic interaction between paclitaxel and roscovitine as well as PHA767491, two compounds known to affect DNA replication origins. Other small-molecule inhibitors with overlapping mechanisms, namely CINK4, flavopiridol, PD-0332991 and purvalanol, have previously been shown to enhance taxane cytotoxicity or reverse taxane resistance (Zhang et al., 2013; Ingemarsdotter et al., 2015; Bible and Kaufmann, 1997; O'Connor et al., 2002). As such a co-targeting strategy is schedule dependent in most cases, the challenge would be to identify optimum dosing regimens that could yield maximal efficacy and minimal toxicity (Jackson et al., 2007; Shah and Schwartz, 2001). We anticipate the FastFUCCI imaging assay to be a useful preclinical tool in these endeavours.

MATERIALS AND METHODS
Gene construction
A synthetic linker was designed and cloned into pBluescript (pBS) to enable the cloning of the FUCCI reporters [mKO2–hCDT1(30–120) and mAG–hGEM(1–110); GeneArt Gene Synthesis] on either side of and in frame with a T2A sequence. This whole cassette was then dropped from pBS and cloned into a third generation lentiviral plasmid (pBOB), as a BamHI and NotI fragment. An EF1α promoter, to drive robust and constitutive transgene expression, was then cloned into pBOB upstream of the FUCCI cassette as a PacI fragment. Finally, a PGK-PURO cassette was cloned as an NheI fragment to enable *in vitro* selection of transduced cells with puromycin. The essential components of the construct are illustrated in Fig. 1A, full map is in Fig. S1, and all single and two-cutter 6+ nucleotide restriction enzymes with respective positions and actual nucleotide numbers are in Table S1.

Cell lines
Generation of FastFUCCI-expressing cells was performed using VSV-G pseudotyped lentiviral particles as previously described (Rodriguez et al., 2014). Briefly, HEK 293T cells were transfected with pBOB-EF1-FastFUCCI-Puro and packaging plasmids. Supernatant from the culture medium containing virus was then collected and used to transduce human pancreatic cancer MIA PaCa-2 and Panc-1 cells (European Collection of Cell Cultures). Following puromycin selection, polyclonal cell populations were expanded. The identity of both parental and transduced cell lines was

authenticated by STR genotyping. In all experiments, cells were grown in Dulbecco's modified Eagle's medium (DMEM) with 10% foetal bovine serum (GIBCO) and were used up to a maximum of 20 passages. All cell lines were verified to be mycoplasma-free using the Mycoprobe Mycoplasma Detection Kit (R&D Systems).

Chemicals
Nocodazole (Sigma), paclitaxel (Tocris or Cayman Chemical), PHA767491 (Tocris), RO3306 (Calbiochem) and roscovitine (Sigma) were dissolved in dimethylsulphoxide (DMSO, Sigma), kept at −20°C and used within 3 months. The final working DMSO concentration was kept at 0.1%.

Flow cytometry
Cells were fixed with 4% paraformaldehyde and stained with DAPI. Red and green fluorescence were captured by the BD LSR II flow cytometer using a blue octagon detector array (488-nm laser) with 555 long-pass and 575/26 band-pass filters, and 505 long-pass and 530/30 band-pass filters, respectively. DAPI was captured using a UV trigon detector array (355-nm laser) with a 450/50 band-pass filter. 10,000 events were collected, and data were processed using the FlowJo software (Tree Star).

Microscopy
Cells were seeded in glass bottom wells (ibidi GmbH) and were kept in a humidified chamber under cell culture conditions. For each well, images were taken from three or more fields of view, where there were no excessive cell clumps so as to capture cells unaffected by potential cell–cell contact inhibition and to facilitate downstream analyses. Images were acquired with either a Nikon Eclipse TE2000-E microscope with a 20×0.45 NA long-working distance dry objective equipped with a sCMOS Andor Neo camera, or a Carl Zeiss Axio Observer Z1 with a 20×0.8 NA dry objective equipped with an Axiocam 506 CCD camera. With the Nikon microscope, red and green fluorescence were captured using a pE-300[white] CoolLED filtered by Nikon FITC B-2E/C and TRITC G-2E/C filter cubes, respectively. With the Zeiss microscope, they were captured using a pE-4000 CoolLED filtered by Zeiss 38HE and 43HE filter cubes, respectively. To achieve optimal image resolution without excessive illumination, a binning factor of 2 by 2 for the sCMOS camera and 5 by 5 for the CCD camera was applied prior to imaging. Throughout each experiment, the ambient conditions of the imaging platform (e.g. external lighting) were maintained to minimise variations in optical resolution and illumination.

Image processing of time-lapse data
Processing of acquired videos was achieved automatically with a script written for Fiji (Schindelin et al., 2012). First, splitting of fluorescence images as single-channel time-lapse videos was performed using the Bio-Formats plug-in in order to convert files into the universal TIFF format. This processing step would also reduce video size, especially if binning was not applied during acquisition. Second, background subtraction and shading correction were applied to individual fluorescence channels. Depending on microscopy conditions (e.g. illumination source and objective shading effect), either the 'Subtract background' feature in Fiji was applied directly, or the Gaussian filter was used to evaluate and subtract the background. Optionally, the 'Bleach correction' plug-in could be used to further reduce auto-fluorescence. Together, these steps minimised intensity variation due to wide-field illumination and improved the signal-to-noise ratio, thus facilitating downstream analyses. A summary of the image processing pipeline is illustrated in Fig. S2A. Links to relevant scripts are provided below.

Automated cell cycle profiling and analysis
To monitor real-time cell cycle distribution, time-lapse images were processed as described above and were analysed in batch mode using the Columbus™ software (PerkinElmer). Image formatting was performed automatically with a Fiji script, which was designed to create an additional red–green merged channel and include time splicing. The resulting TIFF time-lapse images were then imported to the Columbus™ database using PerkinElmer Insight extension. Nuclear segmentation was performed on the

merged red–green channel, optionally de-noised with Gaussian filtering, to detect all relevant nuclei. Sorting was performed to discard objects at the edges of field of view, as well as abnormally small and large objects by minimum and maximum size filter, respectively. Classification of the red-, yellow- and green-emitting populations was undertaken according to the mean and maximum intensities of the fluorescence within the nuclear area. Thresholds were defined based on the fluorescence charts generated by the Columbus™ interface. Fig. S2B depicts the procedure taken to analyse the data using the Columbus™ software. Scripts for image processing and analysis in this section are available at https://github.com/pmascalchi/FastFUCCI-cellcycle.

Automated single-cell tracking and analysis

For single-cell tracking, images were processed as described above and were analysed in batch mode using the TrackMate plug-in available in the Fiji package (Tinevez et al., 2016). This plug-in operated on a user-specified framework that enabled automation of spot segmentation and frame-to-frame spot-tracking. The Laplacian of Gaussian filter was applied to detect spots, and the Linear Assignment Problem tracker was used to track the movement of detected spots. Elimination of false positives (i.e. tracks with short durations) was performed in the final step of the automated protocol. The output included the *xy* coordinates and the track durations of detected spots, as well as videos with tracking paths for quality control. Batch analysis of videos was achieved using the AutoClick Robot software (http://autoclick-robot.en.softonic.com), which allowed automatic mouse clicks and keyboard inputs, complemented with a customised Fiji script to manage sequential video opening, exported data handling and file formatting. Scripts for image processing and analysis in this section are available at https://github.com/pmascalchi/FastFUCCI-tracking.

Quantitative fluorescence-based microscopy

Cells were fixed on glass bottom wells (ibidi GmbH) with 4% paraformaldehyde, immunostained and processed as previously described (Koh et al., 2015). Briefly, images were captured using the iCys laser scanning cytometer (CompuCyte). A digital image was generated for each photomultiplier on a pixel-to-pixel basis. Objects were scored based on preset signal thresholds. The output was processed by the iCys software.

Antibodies

Primary antibodies against c-caspase 3 (#9664, 1:400), cyclin B1 (#4135, 1:1000) and pHH3 (#3377, 1:1600) were from Cell Signaling Technology. γH2AX (#05-636, 1:2500) was from Millipore. Secondary antibodies conjugated to Alexa Fluor 488 (#4408, #4412) and Alexa Fluor 647 (#4410, #4414) were from Cell Signaling Technology and were used at 1:1000.

Cytotoxicity and long-term cell proliferation assays

For sulforhodamine B cytotoxicity assays, cells were fixed with trichloroacetic acid following treatment and were stained with sulforhodamine B dye. Fluorescent readout was obtained using the Infinite 200 PRO microplate reader (Tecan) at excitation and emission wavelengths of 488 nm and 585 nm, respectively. For long-term cell proliferation assays, cells were first subjected to DMSO or paclitaxel treatment for 24 h. Cell viability was then determined using Trypan Blue exclusion, and equal numbers of viable cells were reseeded in fresh medium containing DMSO, roscovitine or PHA767491. After 2 weeks, cells were fixed and stained with 0.2% Crystal Violet (Sigma). Crystal Violet was solubilised using 10% acetic acid and the absorbance was measured at 590 nm using the PHERAStar plate reader (BMG LABTECH). The Bliss additivity prediction was derived from $R_{AB\ Bliss}(a,b)=E_A(a)\bullet E_B(b)$, where R denotes the reference effect, E denotes the observed effect, A and B denote the agents of interest, *a* and *b* denote their respective concentration.

References

Bekier, M. E., Fischbach, R., Lee, J. and Taylor, W. R. (2009). Length of mitotic arrest induced by microtubule-stabilizing drugs determines cell death after mitotic exit. *Mol. Cancer Ther.* **8**, 1646-1654.

Bible, K. C. and Kaufmann, S. H. (1997). Cytotoxic synergy between flavopiridol (NSC 649890, L86-8275) and various antineoplastic agents: the importance of sequence of administration. *Cancer Res.* **57**, 3375-3380.

Boutros, M., Heigwer, F. and Laufer, C. (2015). Microscopy-based high-content screening. *Cell* **163**, 1314-1325.

Chirieleison, S. M., Bissell, T. A., Scelfo, C. C., Anderson, J. E., Li, Y., Koebler, D. J. and Deasy, B. M. (2011). Automated live cell imaging systems reveal dynamic cell behavior. *Biotechnol. Prog.* **27**, 913-924.

Chittajallu, D. R., Florian, S., Kohler, R. H., Iwamoto, Y., Orth, J. D., Weissleder, R., Danuser, G. and Mitchison, T. J. (2015). In vivo cell-cycle profiling in xenograft tumors by quantitative intravital microscopy. *Nat. Methods* **12**, 577-585.

Dan, S., Okamura, M., Mukai, Y., Yoshimi, H., Inoue, Y., Hanyu, A., Sakaue-Sawano, A., Imamura, T., Miyawaki, A. and Yamori, T. (2012). ZSTK474, a specific phosphatidylinositol 3-kinase inhibitor, induces G1 arrest of the cell cycle in vivo. *Eur. J. Cancer* **48**, 936-943.

Enriquez-Navas, P. M., Kam, Y., Das, T., Hassan, S., Silva, A., Foroutan, P., Ruiz, E., Martinez, G., Minton, S., Gillies, R. J. et al. (2016). Exploiting evolutionary principles to prolong tumor control in preclinical models of breast cancer. *Sci. Transl. Med.* **8**, 327ra24.

Gascoigne, K. E. and Taylor, S. S. (2008). Cancer cells profound intra- and interline variation following prolonged exposure to antimitotic drugs. *Cancer Cell* **14**, 111-122.

Gascoigne, K. E. and Taylor, S. S. (2009). How do anti-mitotic drugs kill cancer cells? *J. Cell Sci.* **122**, 2579-2585.

Hamilton, N. (2009). Quantification and its applications in fluorescent microscopy imaging. *Traffic* **10**, 951-961.

Honda-Uezono, A., Kaida, A., Michi, Y., Harada, K., Hayashi, Y., Hayashi, Y. and Miura, M. (2012). Unusual expression of red fluorescence at M phase induced by anti-microtubule agents in HeLa cells expressing the fluorescent ubiquitination-based cell cycle indicator (Fucci). *Biochem. Biophys. Res. Commun.* **428**, 224-229.

Huang, H.-C., Shi, J., Orth, J. D. and Mitchison, T. J. (2009). Evidence that mitotic exit is a better cancer therapeutic target than spindle assembly. *Cancer Cell* **16**, 347-358.

Ingemarsdotter, C. K., Tookman, L. A., Browne, A., Pirlo, K., Cutts, R., Chelela, C., Khurrum, K. F., Leung, E. Y., Dowson, S., Webber, L. et al. (2015). Paclitaxel resistance increases oncolytic adenovirus efficacy via upregulated CAR expression and dysfunctional cell cycle control. *Mol. Oncol.* **9**, 791-805.

Jackson, J. R., Patrick, D. R., Dar, M. M. and Huang, P. S. (2007). Targeted anti-mitotic therapies: can we improve on tubulin agents? *Nat. Rev. Cancer* **7**, 107-117.

Kaida, A., Sawai, N., Sakaguchi, K. and Miura, M. (2011). Fluorescence kinetics in HeLa cells after treatment with cell cycle arrest inducers visualized with Fucci (fluorescent ubiquitination-based cell cycle indicator). *Cell Biol. Int.* **35**, 359-363.

Koh, S.-B., Courtin, A., Boyce, R. J., Boyle, R. G., Richards, F. M. and Jodrell, D. I. (2015). CHK1 inhibition synergizes with gemcitabine initially by destabilizing the DNA replication apparatus. *Cancer Res.* **75**, 3583-3595.

Marcus, J. M., Burke, R. T., Desisto, J. A., Landesman, Y. and Orth, J. D. (2015). Longitudinal tracking of single live cancer cells to understand cell cycle effects of the nuclear export inhibitor, selinexor. *Sci. Rep.* **5**, 14391.

Marshall, J. L. (2012). Maximum-tolerated dose, optimum biologic dose, or optimum clinical value: dosing determination of cancer therapies. *J. Clin. Oncol.* **30**, 2815-2816.

O'connor, D. S., Wall, N. R., Porter, A. C. G. and Altieri, D. C. (2002). A p34(cdc2) survival checkpoint in cancer. *Cancer Cell* **2**, 43-54.

Ogden, A., Rida, P. C. G., Knudsen, B. S., Kucuk, O. and Aneja, R. (2015). Docetaxel-induced polyploidization may underlie chemoresistance and disease relapse. *Cancer Lett.* **367**, 89-92.

Orth, J. D., Tang, Y., Shi, J., Loy, C. T., Amendt, C., Wilm, C., Zenke, F. T. and Mitchison, T. J. (2008). Quantitative live imaging of cancer and normal cells treated with Kinesin-5 inhibitors indicates significant differences in phenotypic responses and cell fate. *Mol. Cancer Ther.* **7**, 3480-3489.

Orth, J. D., Loewer, A., Lahav, G. and Mitchison, T. J. (2012). Prolonged mitotic arrest triggers partial activation of apoptosis, resulting in DNA damage and p53 induction. *Mol. Biol. Cell* **23**, 567-576.

Rieder, C. L. and Maiato, H. (2004). Stuck in division or passing through: what happens when cells cannot satisfy the spindle assembly checkpoint. *Dev. Cell* **7**, 637-651.

Rodriguez, E., Mannion, L., D'santos, P., Griffiths, M., Arends, M. J., Brindle, K. M. and Lyons, S. K. (2014). Versatile and enhanced tumour modelling in mice via somatic cell transduction. *J. Pathol.* **232**, 449-457.

Saitou, T. and Imamura, T. (2016). Quantitative imaging with Fucci and mathematics to uncover temporal dynamics of cell cycle progression. *Dev. Growth Differ.* **58**, 6-15.

Sakaue-Sawano, A., Kurokawa, H., Morimura, T., Hanyu, A., Hama, H., Osawa, H., Kashiwagi, S., Fukami, K., Miyata, T., Miyoshi, H. et al. (2008). Visualizing spatiotemporal dynamics of multicellular cell-cycle progression. *Cell* **132**, 487-498.

Sakaue-Sawano, A., Kobayashi, T., Ohtawa, K. and Miyawaki, A. (2011). Drug-induced cell cycle modulation leading to cell-cycle arrest, nuclear mis-segregation, or endoreplication. *BMC Cell Biol.* **12**, 2.

Schindelin, J., Arganda-Carreras, I., Frise, E., Kaynig, V., Longair, M., Pietzsch, T., Preibisch, S., Rueden, C., Saalfeld, S., Schmid, B. et al. (2012). Fiji: an open-source platform for biological-image analysis. *Nat. Methods* **9**, 676-682.

Shah, M. A. and Schwartz, G. K. (2001). Cell cycle-mediated drug resistance: an emerging concept in cancer therapy. *Clin. Cancer Res.* **7**, 2168-2181.

Shi, J., Orth, J. D. and Mitchison, T. (2008). Cell type variation in responses to antimitotic drugs that target microtubules and kinesin-5. *Cancer Res.* **68**, 3269-3276.

Singh, S., Carpenter, A. E. and Genovesio, A. (2014). Increasing the content of high-content screening: an overview. *J. Biomol. Screen.* **19**, 640-650.

Tao, W., South, V. J., Zhang, Y., Davide, J. P., Farrell, L., Kohl, N. E., Sepp-Lorenzino, L. and Lobell, R. B. (2005). Induction of apoptosis by an inhibitor of the mitotic kinesin KSP requires both activation of the spindle assembly checkpoint and mitotic slippage. *Cancer Cell* **8**, 49-59.

Tinevez, J. Y., Perry, N., Schindelin, J., Hoopes, G. M., Reynolds, G. D., Laplantine, E., Bednarek, S. Y., Shorte, S. L. and Eliceiri, K. W. (2016). TrackMate: an open and extensible platform for single-particle tracking. *Methods*, In press [doi:10.1016/j.ymeth.2016.09.016].

Vakifahmetoglu, H., Olsson, M. and Zhivotovsky, B. (2008). Death through a tragedy: mitotic catastrophe. *Cell Death Differ.* **15**, 1153-1162.

Vassilev, L. T., Tovar, C., Chen, S., Knezevic, D., Zhao, X., Sun, H., Heimbrook, D. C. and Chen, L. (2006). Selective small-molecule inhibitor reveals critical mitotic functions of human CDK1. *Proc. Natl. Acad. Sci. USA* **103**, 10660-10665.

Walling, M. A. and Shepard, J. R. E. (2011). Cellular heterogeneity and live cell arrays. *Chem. Soc. Rev.* **40**, 4049-4076.

Weaver, B. A. A. and Cleveland, D. W. (2005). Decoding the links between mitosis, cancer, and chemotherapy: the mitotic checkpoint, adaptation, and cell death. *Cancer Cell* **8**, 7-12.

Yano, S., Tazawa, H., Hashimoto, Y., Shirakawa, Y., Kuroda, S., Nishizaki, M., Kishimoto, H., Uno, F., Nagasaka, T., Urata, Y. et al. (2013). A genetically engineered oncolytic adenovirus decoys and lethally traps quiescent cancer stem-like cells in S/G2/M phases. *Clin. Cancer Res.* **19**, 6495-6505.

Zhang, X.-H., Cheng, Y., Shin, J.-Y., Kim, J.-O., Oh, J.-E. and Kang, J.-H. (2013). A CDK4/6 inhibitor enhances cytotoxicity of paclitaxel in lung adenocarcinoma cells harboring mutant KRAS as well as wild-type KRAS. *Cancer Biol. Ther.* **14**, 597-605.

Zielke, N. and Edgar, B. A. (2015). FUCCI sensors: powerful new tools for analysis of cell proliferation. *Wiley Interdiscip. Rev. Dev. Biol.* **4**, 469-487.